https://doi.org/10.5194/egusphere-2026-40
Preprint. Discussion started: 15 January 2026

Pressure drag produced by trapped lee waves and propagating mountain waves under nonlinear conditions

Jose Luis Argain [1]

[1]Departamento de Física, FCT, Universidade do Algarve, Campus de Gambelas, 8005-139 Faro, Portugal

Correspondence: jargain@ualg.pt

Abstract. The behaviour of the pressure drag generated by trapped lee waves and upward-propagating internal waves in non-hydrostatic, stratified flow over a mountain ridge is investigated as a function of nonlinearity. A two-layer atmosphere is adopted, with piecewise-constant static stability and a uniform wind profile. The lower layer, between the surface and $z = H$, has stability N_1, and the upper layer extends indefinitely above with stability N_2, where $N_2 < N_1$. Simulations are performed with a numerical model suitable for flows ranging from the microscale to the mesoscale, and nonlinearity is varied solely by increasing the mountain height. Linear reference values are obtained from a previously established linear framework for two-layer trapped and propagating mountain-wave drag. Two configurations are considered: (i) one in which trapped-lee-wave drag dominates over the drag due to propagating waves, and (ii) another in which the two components are of comparable magnitude. A set of diagnostics is introduced to clarify the physical processes associated with increasing nonlinearity. The results show that, as nonlinearity increases, the evolution of the total drag and its components is controlled not only by the amplitude of the trapped lee waves, but above all by the waveguide guiding efficiency. This efficiency determines whether the energy extracted from the incident flow through its interaction with the orography is largely retained and recycled within the trapped mode, or instead is transferred earlier to propagating components and to processes associated with detuning and saturation. These findings may have implications for drag parametrisation in global climate and weather-prediction models.

Keywords: propagating gravity waves; trapped lee waves; resonance; non-hydrostatic effects; linear theory.

1 Introduction

Orographic internal gravity waves impose a pressure drag on the terrain that excites them. This terrain exerts an equal and opposite force on the atmosphere (by Newton's third law) which, because air is a fluid, may be distributed over considerable vertical and horizontal distances. In most cases, the ridges that generate these waves have typical widths smaller than the grid spacing of weather and climate models, so they are rarely resolved. For this reason, the drag must be represented by parametrisations that specify both its magnitude and its spatial allocation (Stensrud, 2009). Over the past decades, a coherent framework has been developed for hydrostatic, vertically propagating gravity waves, providing the physical basis for modern orographic-drag schemes (Phillips, 1984; Shutts and Gadian, 1999). Within this largely linear theory, closed-form expressions for the total drag can often be derived (Smith, 1979; Phillips, 1984; Teixeira and Miranda, 2006). Most classic studies adopted

https://doi.org/10.5194/egusphere-2026-40
Preprint. Discussion started: 15 January 2026

the hydrostatic approximation because mesoscale non-hydrostatic effects are often modest, and the hydrostatic assumption greatly simplifies the analysis.

However, as wind speeds increase and/or static stability decreases, parts of the response become distinctly non-hydrostatic. In the hydrostatic limit, all forced components propagate vertically; under non-hydrostatic conditions, high-wavenumber components become evanescent and do not transport momentum upward, whereas longer waves can still propagate and contribute to drag. If an evanescent layer overlies a propagating layer, strong reflection may trap wave energy, leading to resonance and enhanced drag, alongside partial-reflection effects that may also occur under hydrostatic assumptions (Leutbecher, 2001; Teixeira and Miranda, 2005).

Most atmospheric flows are nonlinear, so it is essential to understand how gravity-wave-induced drag behaves under such conditions. In the hydrostatic regime, this question has received considerable attention. Lilly and Klemp 1979 solved Long's equation to show how finite amplitude and terrain asymmetry can amplify the wave response and the resulting drag. Smith 1989 reviewed hydrostatic airflow over mountains, proposed drag scalings, and clarified the limits of linear theory for different topographic profiles. Durran 1990 synthesised key results for drag in linear hydrostatic flow and discussed how atmospheric structure and finite-amplitude effects modulate it. Olafsson and Bougeault 1996 examined drag enhancement with increasing nonlinearity and the transition to wave breaking in more realistic profiles. Miranda and James 1992 further showed that, for nondimensional mountain height $Nh_0/U \sim O(1)$, a breaking regime can develop and substantially enhance drag relative to its linear reference, even for constant N and U.

By contrast, drag behaviour in non-hydrostatic flows under nonlinear conditions has received less attention. Peltier and Clark 1983 simulated 2D and 3D nonlinear mountain waves, documenting amplification regimes, harmonic generation, and transitions to breaking, all with direct implications for drag. Lott and Teixeira 2016 analysed how nonlinear intensification of trapped-lee-wave modes and their interaction with critical levels modify momentum flux and, consequently, the perceived drag as amplitude increases. Vosper 2004 demonstrated that, in boundary-layer inversions, linear theory underestimates wave amplitudes when horizontal wavelengths are short relative to the terrain width, and that large amplitudes can trigger separation and rotor formation, implying enhanced drag and significant regime shifts as nonlinearity grows. Doyle et al. 2011, drawing on strongly nonlinear T-REX simulations, reported how wave intensification and breaking, including trapped-wave and rotor patterns, modulate momentum fluxes and drag across a range of forcing strengths. Nevertheless, a comprehensive study that explicitly maps drag as a function of nonlinearity in non-hydrostatic flows with trapped lee waves remains lacking.

In Teixeira et al. 2013a, a two-layer atmosphere with piecewise-constant parameters of the type originally considered by Scorer 1949 is used to evaluate the trapped-lee-wave drag and the drag associated with vertically propagating waves, and to compare the magnitude of these two components. It is shown that, in some circumstances, trapped-lee-wave drag can be comparable to, or even larger than, the drag due to vertically propagating waves, and substantially larger than the drag predicted for a hydrostatic atmosphere with a constant Scorer parameter equal to that in the lower layer. These results have direct implications for gravity-wave drag parametrisations (Lott, 1998). In Teixeira et al. 2013b, the drag associated with lee waves trapped at an inversion capping a neutrally stratified layer, together with the drag due to waves propagating in the stably stratified layer aloft, is investigated. As in Teixeira et al. 2013a, trapped-lee-wave drag is found to be comparable to

https://doi.org/10.5194/egusphere-2026-40
Preprint. Discussion started: 15 January 2026

the propagating-wave contribution and larger than the one-layer hydrostatic reference drag. However, unlike the configuration considered in Teixeira et al. 2013a and consistent with the discussion in Vosper 2004, only a single trapped-lee-wave mode exists in this case, implying that only one drag maximum occurs in parameter space.

The lack of studies addressing how trapped-lee-wave drag and the drag due to vertically propagating waves evolve as nonlinearity increases provides the main motivation for the present work. Accordingly, this paper investigates in detail how total drag and its two components depend on nonlinearity in non-hydrostatic flows that generate trapped lee waves, using a numerical model (FLEX) suitable for simulating flows from the microscale to the mesoscale. The model has been previously validated against experimental and field data relevant to engineering and meteorological applications. Two cases are examined, guided by the linear theoretical results of Teixeira et al. 2013a cited above: (i) a configuration in which trapped-lee-wave drag dominates over the drag produced by propagating internal waves, and (ii) a configuration in which the two drag components are of comparable magnitude. The simplicity of the atmospheric set-up adopted in this theoretical model facilitates a clearer separation of the complex effects associated with nonlinearity.

This article is organised as follows. Section 2 describes the linear model used to compute trapped-lee-wave drag and the drag associated with vertically propagating waves in the linear regime. Section 3 introduces the theoretical model, and Section 4 describes the two studied cases based on this model. Section 5 explains the diagnostic parameters employed to investigate how increasing nonlinearity affects drag. Section 6 describes the non-hydrostatic numerical model. Section 7 presents illustrative numerical experiments showing the behaviour of the drag and of the diagnostics as functions of nonlinearity for the two configurations introduced above, and provides a detailed analysis of the underlying physical mechanisms. Finally, Section 8 offers concluding remarks and discusses the main implications of the results.

2 Theoretical model

The linear theoretical model of Teixeira et al. 2013a was developed for an inviscid, stationary, non-rotating, stratified flow over a 2D mountain ridge of relatively small amplitude, aligned in the y direction. The flow is of sufficiently large scale to be approximately inviscid (i.e. not a boundary-layer flow), but of sufficiently small scale for the rotation of the Earth to be negligible. If the equations of motion under the Boussinesq approximation are linearised about a reference mean state, combined appropriately, and the dependent variables are expressed as Fourier integrals in x, it can be shown that the Fourier transform of the vertical-velocity perturbation, $\widehat{w}$, satisfies

$$\frac{\partial^2 \widehat{w}}{\partial z^2} + \left(l^2 - k^2\right) \widehat{w} = 0, \tag{1}$$

where

$$l = \left(\frac{N^2}{U^2} - \frac{1}{U} \frac{d^2 U}{dz^2} \right)^{1/2}, \tag{2}$$

is the Scorer parameter of the atmosphere. Here, k is the horizontal wavenumber in the x direction, $N^2(z) > 0$ is the static stability of the reference state, and $U(z)$ is the incoming wind speed (aligned with x and therefore perpendicular to the ridge).

https://doi.org/10.5194/egusphere-2026-40
Preprint. Discussion started: 15 January 2026

A two-layer atmosphere similar to that prescribed by Scorer 1949 is assumed, with the lower layer between $z = 0$ and $z = H$ and the upper layer extending indefinitely above. In each layer, both the static stability N and the wind speed U are taken to be constant, so the corresponding Scorer parameters are also constant. Although the formulation allows different values of U in each layer, in this study U is taken to be constant throughout. The Scorer parameter is therefore discontinuous at $z = H$. The static stability and Scorer parameter in the lower layer are denoted by N_1^2 and l_1, respectively, while in the upper layer the corresponding quantities are N_2^2 and l_2. Since trapped lee waves (TLW hereafter) are the main focus of the present study, $l_2 < l_1$ is always assumed, which is a necessary condition for wave trapping.

In this atmospheric structure, three possibilities exist: waves may propagate vertically in both layers, they may propagate only in the lower layer, or they may be evanescent in both layers. The pressure drag force directed across the ridge, per unit length in the cross-flow (spanwise) direction, is defined as

$$D = \int_{-\infty}^{+\infty} p_1(z=0)\,\frac{\partial h}{\partial x}\,dx, \tag{3}$$

where p_1 is the pressure perturbation in the lower layer and $h(x)$ is the surface elevation. In this study, the orography is assumed to be symmetric and bell-shaped:

$$h(x) = \frac{h_0}{1+(x/a)^2}, \tag{4}$$

where h_0 is the maximum height and a is the half-width. The total drag D can be decomposed as

$$D = D_{pw} + D_{tlw}, \tag{5}$$

with D_{pw} associated with internal waves that propagate in the upper layer ($z > H$), and D_{tlw} associated with TLW confined to the lower layer ($z < H$). In this framework, D_{pw} receives contributions from wavenumbers satisfying $k^2 < l_2^2$ (propagating in the upper layer), whereas D_{tlw} receives contributions from wavenumbers satisfying $k^2 > l_2^2$ (evanescent in the upper layer). The dependence of D and of the TLW wavelength λ_0 on $l_1 H/\pi$ was compared with numerical simulations, showing very good agreement.

Using this model, Teixeira et al. 2013a investigated the behaviour of the drag D, normalised by its hydrostatic single-layer reference value D_0 ($D_0 = 0.25\pi\rho U N_1 h_0^2$, where ρ is the air density), as a function of l_2/l_1 and the corresponding non-dimensional interface height $l_1 H/\pi$, for selected values of the non-dimensional ridge width $l_1 a$ and wind-speed ratio U_1/U_2. When $l_2/l_1 \to 1$, the propagating-wave drag approaches 1 (under approximately hydrostatic conditions) and the TLW drag vanishes. As l_2/l_1 decreases, the propagating-wave drag develops an oscillatory dependence on $l_1 H/\pi$, with maxima of increasing magnitude due to constructive interference of reflected waves in the lower layer. The TLW drag exhibits local maxima associated with each resonant TLW mode, occurring for small l_2/l_1 and at slightly larger values of $l_1 H$ than the propagating-wave maxima. As $l_1 a$ decreases (i.e. as the response becomes more non-hydrostatic), the propagating-wave drag decreases and the region of non-zero TLW drag extends to larger values of l_2/l_1. These results were confirmed by numerical simulations for $l_2/l_1 = 0.2$ and $U_1/U_2 = 1$, using the FLEX numerical model. This is precisely the configuration considered here to study the effect of nonlinearity on TLW.

https://doi.org/10.5194/egusphere-2026-40
Preprint. Discussion started: 15 January 2026

3 Studied cases

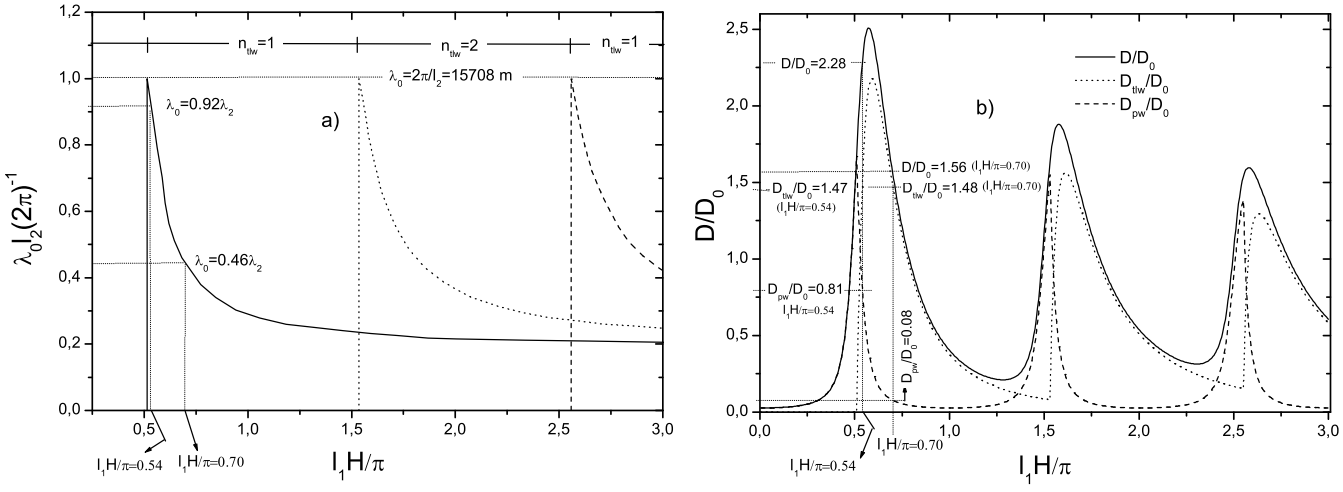

Figure 1. Linear-theory results used to select the two TLW configurations analysed in the nonlinear simulations. The results shown correspond to $l_2/l_1 = 0.2$ and $U_1/U_2 = 1$. (a) TLW horizontal wavelength λ_0 (for the first three trapped modes, labelled by n_{tlw}) normalised by its maximum attainable value $\lambda_2 = 2\pi/l_2$, as a function of the non-dimensional waveguide depth $\hat{H} = l_1 H/\pi$. (b) Corresponding total drag D/D_0 in a distinctly non-hydrostatic regime ($l_1 a = 2$) and its decomposition into trapped-wave and propagating-wave contributions, D_{tlw}/D_0 and D_{pw}/D_0, versus $\hat{H}$, highlighting the resonance peaks associated with each trapped mode. The vertical markers indicate the two parameter choices adopted in this study, $\hat{H} = 0.54$ and 0.70, for which λ_0 and the relative importance of D_{tlw} and D_{pw} differ substantially.

Figures 1a and 1b are reproduced from the analytical model of Teixeira et al. 2013a. Figure 1a shows the trapped-lee-wave (TLW) horizontal wavelength λ_0, normalised by its maximum attainable value $\lambda_2 = 2\pi/l_2$, as a function of the non-dimensional waveguide depth $\hat{H}$. Results are shown for the first three TLW modes, $n_{tlw} = 1, 2$, and 3. Here $\hat{H} = l_1 H/\pi$. As $\hat{H}$ increases, successive trapped modes become available. One TLW mode exists for $0.5 \leq \hat{H} < 1.5$, two modes for $1.5 \leq \hat{H} < 2.5$, and three modes for $\hat{H} \geq 2.5$. For each newly available mode, λ_0/λ_2 departs from unity; as $\hat{H}$ increases further, it asymptotically approaches l_2/l_1 (equal to 0.2 in the present set-up). In this model, n_{tlw} and λ_0 are independent of the non-dimensional mountain half-width $l_1 a$ (here $l_1 a = 2$) and of the wind-speed ratio U_1/U_2 (here $U_2 = U_1$).

Figure 1b shows the theoretical dependence of the normalised total drag D/D_0 and its decomposition into trapped-lee-wave drag D_{tlw}/D_0 and propagating-wave drag D_{pw}/D_0, as functions of $\hat{H}$, for $l_2/l_1 = 0.2$ and $l_1 a = 2$. In this distinctly non-hydrostatic regime, D_{tlw} can be comparable to D_{pw} and can exceed it over some intervals, so TLW drag may represent a substantial fraction of the total drag. The maxima of D_{pw}/D_0 associated with each trapped mode occur near $\hat{H} = 0.5 + n$ (with n an integer), whereas the maxima of D_{tlw}/D_0 are shifted to slightly larger values of $\hat{H}$. Away from the immediate vicinity of $\hat{H} = 0.5 + n$, D_{tlw}/D_0 generally exceeds D_{pw}/D_0. This highlights the potential importance of TLW drag in non-hydrostatic two-layer configurations, relative to the classical hydrostatic one-layer reference.

https://doi.org/10.5194/egusphere-2026-40
Preprint. Discussion started: 15 January 2026

To examine how D/D_0, D_{tlw}/D_0, and D_{pw}/D_0 evolve with nonlinearity, nonlinearity is parameterised by the non-dimensional mountain height

$$\hat{h}_0 = l_1 h_0. \tag{6}$$

Thus, nonlinearity is varied exclusively by changing h_0, while N_1 and U are held fixed.

Two cases are selected from the linear-theory map of Teixeira et al. 2013a: i) $\hat{H} = 0.70$ and ii) $\hat{H} = 0.54$ (indicated in the figures). In the case i), trapped-lee-wave drag dominates the total drag (about 95% of D in the linear reference), and the TLW wavelength is close to its maximum value ($\lambda_0 = 0.92\lambda_2 = 14451$ m). In the case ii), the TLW contribution is smaller (about 64% of D in the linear reference), and the propagating-wave contribution is correspondingly more significant. In this case, $\lambda_0 = 0.46\lambda_2 = 7226$ m, i.e. approximately half the value obtained for $\hat{H} = 0.70$. Finally, to isolate the role of nonlinearity as cleanly as possible, only single-mode TLW configurations are considered in the present study.

4 Numerical model

This study uses the FLEX numerical model, a two-dimensional micro-to-mesoscale model formulated in orthogonal curvilinear coordinates, which has been used previously to investigate resonant mountain-wave flows (Argain et al., 2009; Teixeira and Miranda, 2005; Teixeira et al., 2008, 2013a, b). All simulations employ a horizontal grid spacing of $\Delta x = 200$ m and a vertical grid spacing of $\Delta z = 24$ m. The background wind is uniform with $U = 10\,\mathrm{m\,s^{-1}}$. Static stability is prescribed as $N_1 = 0.02\,\mathrm{s^{-1}}$ in the lower layer and $N_2 = 0.004\,\mathrm{s^{-1}}$ in the upper layer, giving $N_2/N_1 = 0.2$ and, for uniform U, $l_2/l_1 = 0.2$.

The mountain has the bell-shaped profile (4) and half-width $a = 1000$ m, which yields $l_1 a = 2$ and therefore a strongly non-hydrostatic response. The mountain height is varied to control nonlinearity, from $h_0 = 10$ m (weakly nonlinear; $\hat{h}_0 = l_1 h_0 = 0.02$) up to $h_0 = 500$ m (strongly nonlinear; $\hat{h}_0 = 1$).

The vertical domain extends up to six hydrostatic vertical wavelengths, $\lambda_{z0} = 2\pi/l_1$. The mountain is centred at $x = 0$. The upstream domain length is $15a$, and the downstream domain extends to approximately seven TLW wavelengths, λ_0, measured in the linear reference regime. The model time step is $\Delta t = 1$ s, and simulations are integrated for $\approx 500a/U$ (about 14 h).

A sponge layer is applied near the top boundary over a depth of approximately $2.5\,\lambda_{z0}$. At the downstream boundary, the radiation condition of Raymond and Kuo (1984) is imposed. In addition, sponge layers spanning 15 and 30 grid points are applied at the upstream and downstream boundaries, respectively.

For the two studied TLW configurations ($\hat{H} = 0.54$ and $\hat{H} = 0.70$), $\hat{h}_0$ varies between 0.02 and 1. Larger values are not considered because, as shown later, TLW effects on the drag variability (the main focus of this work) become unimportant for $\hat{h}_0 > 1$.

5 Diagnostic parameters

To study the behaviour of D and its components as functions of the non-dimensional mountain height $\hat{h}_0$, a set of diagnostic parameters is introduced.

https://doi.org/10.5194/egusphere-2026-40
Preprint. Discussion started: 15 January 2026

5.1 Displacement amplitude and wavelength

In linear, adiabatic, and reversible flow, the wave field can be visualised using the isentropic vertical displacement $\eta(x,z)$ inferred from the potential-temperature perturbation $\theta'(x,z)$. In that limit, $\eta(x,z)$ and $w'(x,z)$ have similar spatial structure, and the maximum TLW displacement amplitude, $\eta_{\max}$, can be estimated directly from $\eta(x,z)$. As $\hat{h}_0$ increases, the relationship between η and w' becomes nonlinear, and η no longer represents the actual parcel displacement. For this reason, $\eta_{\max}$ is estimated here from $w'_{\max}$ using

$$\eta_{\max} = \frac{w'_{\max}\lambda_0}{2\pi U} \text{ or, in non-dimensional form, } \frac{\eta_{\max}}{h_0} = \frac{w'_{\max}\lambda_0}{2\pi U h_0}. \tag{7}$$

Here λ_0 is the TLW wavelength in the linear regime ($\hat{h}_0 \ll 1$), so that $k_0 = 2\pi/\lambda_0$ denotes the corresponding linear horizontal wavenumber. This estimate follows from the kinematic relation $w' \approx U\,\partial\eta/\partial x$ and remains meaningful for any degree of nonlinearity because it is based on the directly simulated maximum vertical velocity. To better understand the behaviour of the TLW field, the location of the maximum of η is determined, i.e., $(x_{\eta_{\max}}, z_{\eta_{\max}})$. In the nonlinear regime, the TLW wavelength λ is estimated as the average wavelength of the primary TLW train. The corresponding nonlinear horizontal wavenumber is defined as $k = 2\pi/\lambda$.

5.2 Energy leakage from the waveguide

The vertical wave energy flux per unit area at height z is quantified by the horizontally averaged quantity

$$\overline{p'w'}(z) = \frac{1}{L_x}\int_0^{L_x} p'(x,z)\,w'(x,z)\,dx, \tag{8}$$

where L_x is the horizontal domain length and the overbar denotes a horizontal average. If TLW are well confined within the waveguide, $\overline{p'w'}(z)$ above the waveguide should be small; any non-zero value primarily reflects leakage to propagating components and/or dissipative effects.

At a height z_{top} sufficiently far above the waveguide, the upward energy leakage is estimated by $\overline{p'w'}(z_{top})$. Accordingly, the fraction of energy that escapes the waveguide is defined as

$$S_{pw} = \frac{\left|\overline{p'w'}(z_{top})\right|}{\max_{z\in[0,H]}\left|\overline{p'w'}(z)\right|}, \tag{9}$$

where the denominator is the maximum (in magnitude) of $\overline{p'w'}(z)$ within the waveguide. To characterise structural changes in the TLW field, the locations of the maxima of S_{pw} are also recorded, i.e., $(x_{S_{pw}^{\max}}, z_{S_{pw}^{\max}})$.

5.3 Momentum leakage from the waveguide

The vertical flux of horizontal momentum carried by the waves at height z is computed as

$$\overline{u'w'}(z) = \frac{1}{L_x}\int_0^{L_x} u'(x,z)\,w'(x,z)\,dx. \tag{10}$$

https://doi.org/10.5194/egusphere-2026-40
Preprint. Discussion started: 15 January 2026

The vertical derivative $-\partial\overline{u'w'}(z)/\partial z$ is the local rate of mean-flow acceleration (or deceleration) due to wave momentum deposition. Where $\overline{u'w'}$ decreases with z, the wave field deposits momentum and the mean flow accelerates, and vice-versa.

The fraction of momentum flux that escapes the waveguide is estimated by

$$S_{uw} = \frac{\left|\overline{u'w'}(z_{top})\right|}{\max_{z\in[0,H]}\left|\overline{u'w'}(z)\right|}. \tag{11}$$

A small S_{uw} indicates that the momentum flux has been substantially reduced below z_{top} (by deposition and/or dissipation), implying strong wave–mean-flow coupling. Conversely, $S_{uw} \approx 1$ implies that a significant fraction of the momentum flux reaches z_{top}, consistent with efficient leakage to propagating components. For the same reason as in the case of S_{pw}, we also use the location of the maximum of S_{uw}, i.e., $(x_{S_{uw}^{\max}}, z_{S_{uw}^{\max}})$.

5.4 Energy–momentum coupling

To quantify departures from the linear energy–momentum relationship, the diagnostic parameter $\overline{C}_u$ is introduced as

$$\overline{C}_u = \frac{1}{z_2 - z_1}\int_{z_1}^{z_2} C_u(z)\,dz, \tag{12}$$

where $C_u(z)$ is the local ratio between energy and momentum fluxes,

$$C_u(z) = \frac{\overline{p'w'}(z)}{-\rho\,\overline{u'w'}(z)}. \tag{13}$$

In the linear limit, $C_u(z) \approx U$ within the waveguide. Hence, if $\overline{C}_u$ remains close to U (e.g. deviations $< 10\%$) as $\hat{h}_0$ increases, energy and momentum leakage remain approximately proportional and the response retains a predominantly linear structure.

In this study, $\overline{C}_u$ is evaluated between $z_1 = 0$ and $z_2 = 0.8H$ to avoid sharp flux variations near $z = H$.

5.5 Link between $\eta_{\max}$ and linear drag scaling

In the linear regime, an order-of-magnitude relation in the TLW waveguide is $w'_{\max} \sim \sqrt{D_{tlw}/(\rho H)}$. Combining this with (7) yields

$$\eta_{\max} = \frac{\lambda_0}{2\pi U}\sqrt{\frac{D_{tlw}}{\rho H}}. \tag{14}$$

If D_{tlw} follows the quadratic linear scaling $D_{tlw} \propto \rho N_1 U h_0^2$ (for fixed N_1, U, λ_0, ρ and H), then

$$\eta_{\max} = C h_0 \text{ or } \eta_{\max} = C\hat{h}_0, \tag{15}$$

where C is a constant. Outside the linear regime, this proportionality need not hold.

https://doi.org/10.5194/egusphere-2026-40
Preprint. Discussion started: 15 January 2026

5.6 Retuning induced by mean-flow modification

For fixed H, N_1, λ_0 and U, the lower-layer vertical wavenumber associated with the linear reference mode is

$$m_1 = \sqrt{l_1^2 - k_0^2}, \tag{16}$$

and the modal condition (through $m_1 H$) does not vary with $\hat{h}_0$ in the strictly linear regime.

As $\hat{h}_0$ increases, wave momentum fluxes can generate a non-zero horizontally averaged perturbation wind. Although the imposed reference profile is $U = \text{const.}$, the effective mean wind becomes $U_{\text{eff}}(z, \hat{h}_0) = U + \Delta U(z, \hat{h}_0)$. Assuming a local stationary-wave dispersion relation, the corresponding effective vertical wavenumber is approximated by

$$m_{1\text{eff}}(z, \hat{h}_0) \approx \sqrt{\frac{N_1^2}{U_{\text{eff}}^2(z, \hat{h}_0)} - k^2}, \tag{17}$$

where $k = 2\pi/\lambda$ is computed from the diagnosed nonlinear TLW wavelength λ. The relative change in vertical wavenumber is then

$$\frac{\Delta m_1}{m_1}(z, \hat{h}_0) = \frac{m_{1\text{eff}}(z, \hat{h}_0) - m_1}{m_1}. \tag{18}$$

The mean-flow modification $\Delta U(z, \hat{h}_0)$ is computed as the horizontal average of $u'(x, z)$ at each z:

$$\Delta U(z, \hat{h}_0) = \overline{u'}(z, \hat{h}_0) = \frac{1}{L_x} \int_0^{L_x} u'(x, z, \hat{h}_0)\, dx. \tag{19}$$

In nonlinear flow, quadratic terms can produce a non-oscillatory ($k = 0$) component of u', so that $\overline{u'} \neq 0$. It is useful to distinguish (i) waveform distortion that generates harmonics ($2k$, $3k$, etc.) but may still have $\overline{u'} = 0$, from (ii) an induced mean component with $\overline{u'} \neq 0$. Only the latter contributes to $U_{\text{eff}}(z, \hat{h}_0)$.

The diagnostic $\Delta m_1/m_1$ therefore provides an indirect measure of retuning, quantifying how the effective mode departs from the linear reference as $\hat{h}_0$ increases. In the linear limit ($\hat{h}_0 = 0$), $\Delta m_1/m_1 = 0$ by construction. In what follows, the maximum deviation within the waveguide, $(\Delta m_1)_{\max}/m_1$, is used as a single summary measure.

5.7 Flux-based drag decomposition

The drag D_{pw} is diagnosed from the vertical momentum flux at the top of the domain, which primarily represents propagating-wave (PW) contributions reaching z_{top}:

$$D_{pw} \approx -\rho\, \overline{u'w'}(z_{top}). \tag{20}$$

The residual contribution associated with TLW (and, more generally, processes confined below z_{top}) is then estimated as

$$D_{tlw} \approx D - D_{pw}. \tag{21}$$

This flux-based decomposition is less direct than a spectral separation based on the Scorer parameter, but it provides a simple and physically interpretable estimate of how D_{pw} and D_{tlw} evolve with $\hat{h}_0$ and how their contrast differs between the two studied cases, $\hat{H} = 0.70$ and $\hat{H} = 0.54$.

https://doi.org/10.5194/egusphere-2026-40
Preprint. Discussion started: 15 January 2026

6 Results and discussion

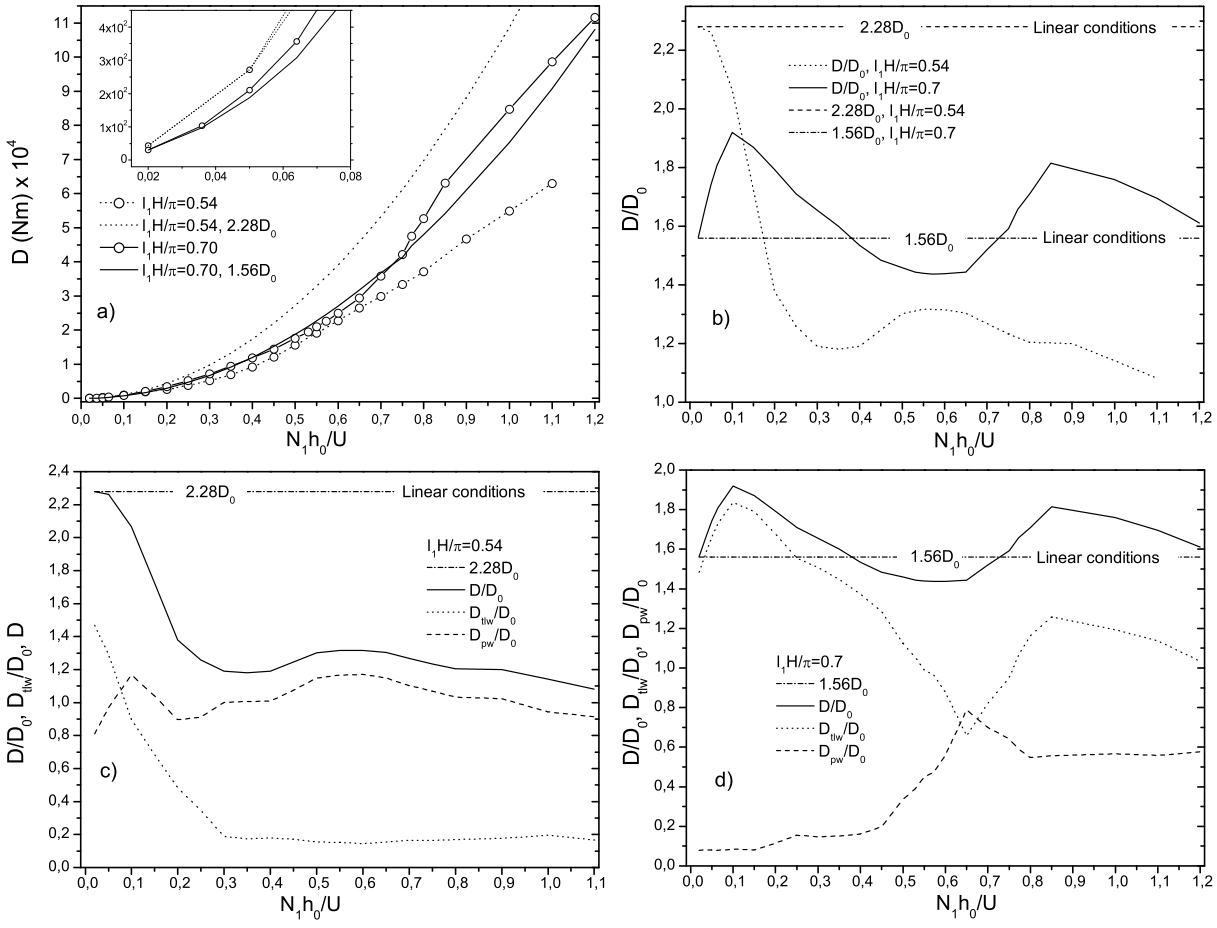

Figure 2. Variation of the pressure drag with nonlinearity ($\hat{h}_0 = N_1 h_0/U$) for the two TLW waveguide configurations $\hat{H} = 0.54$ and $\hat{H} = 0.70$. (a) Absolute drag D together with ideal linear extrapolations (shown as $D = 2.28D_0$ for $\hat{H} = 0.54$ and $D = 1.56D_0$ for $\hat{H} = 0.70$). (b) Same curves normalised by the hydrostatic drag D_0. (c–d) Flux-based partition into propagating-wave drag D_{pw} and trapped-wave contribution $D_{tlw} = D - D_{pw}$.

Because H, N_1, λ_0 and U are fixed, variations in the diagnostics discussed below primarily reflect finite-amplitude effects associated with increasing $\hat{h}_0$ relative to the linear regime (phase shifts, saturation, harmonic generation and mean-flow modification).

Figure 2(a) shows the numerically diagnosed pressure drag D as a function of $\hat{h}_0$ for $\hat{H} = 0.54$ (dotted line) and $\hat{H} = 0.7$ (solid line), together with ideal linear extrapolations $D = 2.28D_0$ and $D = 1.56D_0$, respectively, obtained by assuming linear conditions over the full range of $\hat{h}_0$. Since $D_0 \propto \hat{h}_0^2$ and the linear forcing scales with h_0, D is expected to be approximately quadratic at sufficiently small amplitude; accordingly, $D \propto \hat{h}_0^2$ for very small $\hat{h}_0$, but it departs rapidly from $D = cD_0$. For

https://doi.org/10.5194/egusphere-2026-40
Preprint. Discussion started: 15 January 2026

$\hat{H} = 0.54$, D remains below its linear extrapolation throughout, indicating a progressive loss of waveguide efficiency as $\hat{h}_0$ increases. For $\hat{H} = 0.7$, D initially falls below $1.56D_0$, but it recovers at larger amplitudes and exceeds the linear prediction, suggesting a nonlinear reorganisation that enhances the drag. Overall, the $\hat{H} = 0.7$ case, where D_{tlw} dominates in the linear limit, is less sensitive to increasing $\hat{h}_0$ than the $\hat{H} = 0.54$ case, indicating that D_{pw} is more sensitive to nonlinearity.

Figure 2(b) presents the same curves normalised by D_0. For $\hat{H} = 0.7$, D/D_0 reaches a maximum near $\hat{h}_0 \approx 0.1$, consistent with a modest-amplitude regime in which TLW amplitude benefits from enhanced resonance. For $\hat{h}_0 > 0.1$, D/D_0 decreases and forms a broad minimum ($D/D_0 \approx 1.44$) over $\hat{h}_0 \approx 0.55$–0.65, implying a substantial reduction in TLW coherence and/or guiding efficiency; $\eta_{\max}$ versus $\hat{h}_0$ provides a complementary indicator of this change. For $\hat{h}_0 > 0.65$, D/D_0 increases again, before a second collapse near $\hat{h}_0 \approx 0.85$. The predominance of D_{tlw} over D_{pw} in Figure 2(d) shows that TLWs recover up to $\hat{h}_0 \approx 0.85$ and then collapse again, after which the drag decreases monotonically, confirming the central role of TLWs in this behaviour.

For $\hat{H} = 0.54$, D/D_0 collapses rapidly and remains below the linear extrapolation. This is consistent with Figure 2(c), which shows that, outside the near-linear regime, D_{pw} dominates over D_{tlw}. These results motivate the central hypothesis tested below: in the low-efficiency waveguide ($\hat{H} = 0.54$), D_{tlw} peaks in the near-linear regime and then collapses, being progressively replaced by PWs, whereas in the high-efficiency waveguide ($\hat{H} = 0.7$) strong TLWs persist over a broader range of $\hat{h}_0$, undergoing detuning and saturation but recovering at larger amplitudes while coexisting with an increasing PW contribution.

Figures 3–8 test these hypotheses by linking wave morphology, geometric diagnostics and energy / momentum fluxes to the drag behaviour in Figure 2.

In Figure 3 ($\hat{H} = 0.7$), $\eta(x, z)$ is near-linear at $\hat{h}_0 = 0.02$: monochromatic sinusoidal waves are coherent across the waveguide, with $\eta(x, z)$ maximised near $z \approx H$ and the main crest aligned with the ridge. At $\hat{h}_0 = 0.3$, crest steepening and a slight downstream shift indicate harmonic generation ($2k, 3k, \ldots$) and weak modal detuning linked to mean-flow modification.

By $\hat{h}_0 = 0.5$–0.55, the primary train remains identifiable but becomes strongly modulated: a low-frequency jump/jet develops near the lee slope and a second, relatively clean TLW train emerges downstream. For $\hat{h}_0 = 0.6$–0.8, the first train collapses into large-scale jump-like structures that act as an effective mountain for a well-organised secondary TLW train with smaller λ, displaced several wavelengths downstream. This indicates that the high-efficiency waveguide can reconvert part of the finite-amplitude response into coherent trapped waves, maintaining a significant trapped contribution to the drag even at large amplitude.

In Figure 4 ($\hat{H} = 0.54$), the near-linear case ($\hat{h}_0 = 0.02$) is already less clean than in Figure 3: amplitudes are smaller, decay with height is stronger, and interference with PWs above the waveguide appears earlier. As $\hat{h}_0$ increases (0.2–0.4), steepening

https://doi.org/10.5194/egusphere-2026-40
Preprint. Discussion started: 15 January 2026

and harmonics develop, but energy leaks upward and downstream more efficiently; the trapped train is damped and disorganised rather than reorganising into a coherent secondary train.

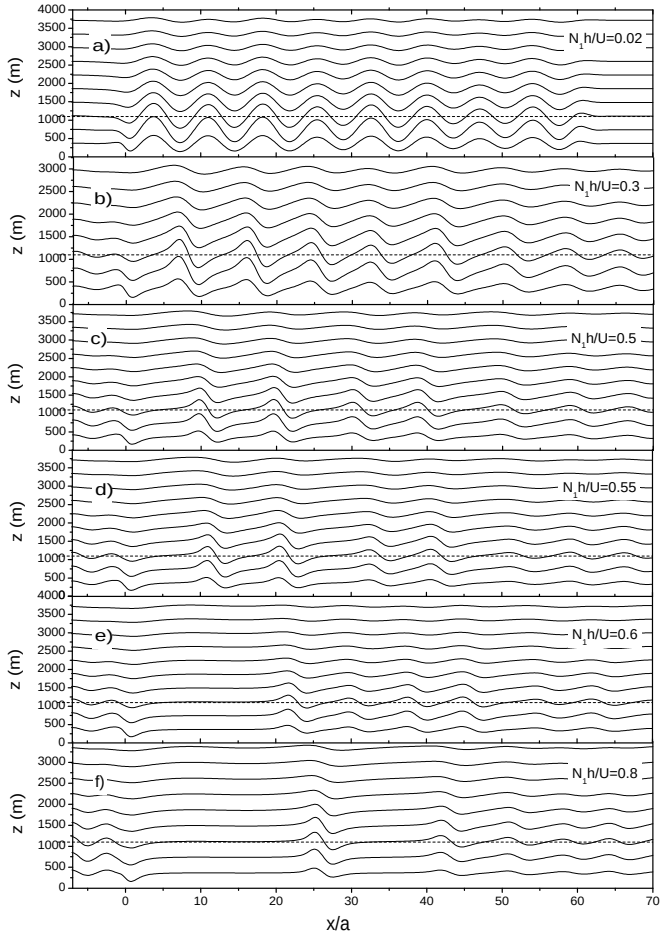

Figure 3. Wave-field evolution in the high-efficiency TLW waveguide case $\hat{H} = 0.70$ as nonlinearity ($\hat{h}_0 = N_1 h_0/U$) increases.

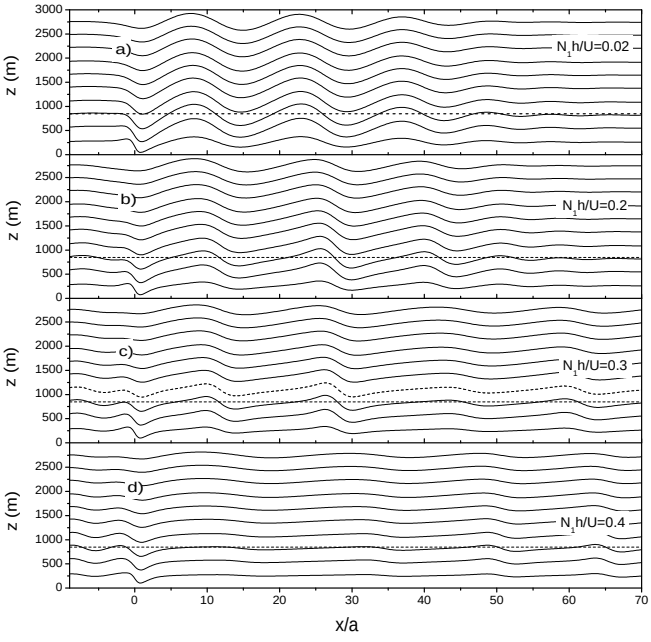

Figure 4. Wave-field evolution in the low-efficiency TLW waveguide case $\hat{H} = 0.54$ as nonlinearity increases.

In Figure 5, the variation of several geometric diagnostic parameters with $\hat{h}_0$ is shown. In Figure 5a, the normalised wavelength, λ/λ_0, increases with $\hat{h}_0$ while the response remains approximately monochromatic. This lengthening persists up to the loss of monochromaticity, which is clearly illustrated in Figures 3d and 4c.

This loss occurs much earlier for $\hat{H} = 0.54$ ($\hat{h}_0 \approx 0.3$ with $\lambda = 1.23\lambda_0$) than for $\hat{H} = 0.7$ ($\hat{h}_0 \approx 0.55$ with $\lambda = 1.38\lambda_0$), consistent with the more rapid collapse of TLW resonance in the low-efficiency waveguide. As can be seen in Figures 3e and 3f (for $\hat{H} = 0.7$), the secondary trapped train that forms after the jump ($\hat{h}_0 > 0.6$) has a smaller λ than that diagnosed at $\hat{h}_0 = 0.55$,

https://doi.org/10.5194/egusphere-2026-40
Preprint. Discussion started: 15 January 2026

when the primary train collapses ($1.38\lambda_0$). This value remains nearly constant ($\lambda \approx 1.06\lambda_0$) until the train disappears at $\hat{h}_0 \approx 1$ (not shown here).

In Figure 5b the maximum relative deviation $(\Delta m_1)_{\max}/m_1$ is shown; as noted above, this quantity directly measures the nonlinear retuning of the mode relative to the linear reference solution and is used only in regimes where the mode remains identifiable (i.e. the spectrum exhibits a dominant peak). As expected, $(\Delta m_1)_{\max}/m_1 \approx 0$ in the linear regime; it becomes negative and increases in magnitude for both cases, reaching about 10% at $\hat{h}_0 \approx 0.3$ for $\hat{H} = 0.54$ and about 20% at $\hat{h}_0 \approx 0.55$ for $\hat{H} = 0.7$ (values of $\hat{h}_0$ at which the primary wave train collapses in each configuration). This progressive increase in the negativity of $\Delta m_1/m_1$ with $\hat{h}_0$ implies a lengthening of λ_z (the effective hydrostatic vertical wavelength), consistent with the increase in λ diagnosed in Figure 5a for both cases. The waveguide selects resonant modes on the basis of the modal condition $m_1 H = n\pi$ together with the Scorer-parameter constraint; if m_1 decreases (because $\Delta U_{\text{eff}} > 0$), the system tends to readjust by selecting quasi-resonant modes that approximately satisfy both the modal condition and the dispersion relation, given the modified U_{eff} and λ. This indicates that waveguide modification (via U_{eff} and λ) promotes a predominantly one-way adjustment that shifts the initially dominant trapped component in (k, m) space; accordingly, the m_1 diagnostic provides the vertical signature of this readjustment, whereas λ provides the observable horizontal signature.

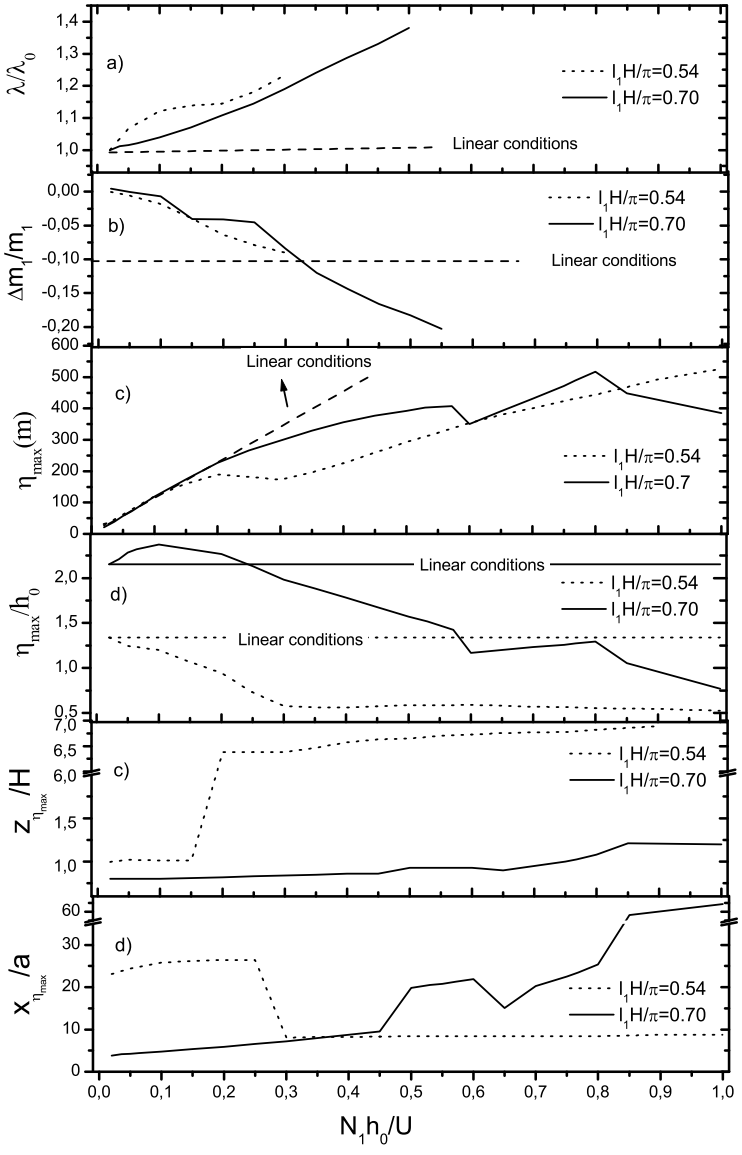

Figure 5. Geometric diagnostics versus nonlinearity ($\hat{h}_0$) for $\hat{H} = 0.54$ and $\hat{H} = 0.70$. (a) Normalised trapped wavelength λ/λ_0. (b) Maximum relative retuning $(\Delta m_1)_{\max}/m_1$. (c) Maximum displacement amplitude $\eta_{\max}$. (d) $\eta_{\max}$ normalised by h_0, compared with the linear reference. (e) Vertical position of $\eta_{\max}$ ($z_{\eta_{\max}}/H$). (f) Downstream position of $\eta_{\max}$ ($x_{\eta_{\max}}/a$).

https://doi.org/10.5194/egusphere-2026-40
Preprint. Discussion started: 15 January 2026

Figure 5c ($\eta_{\max}$ vs. $\hat{h}_0$) shows that, for $\hat{h}_0 \leq 0.15$, $\eta_{\max}$ closely follows the linear predictions derived from $w'_{\max} \propto \sqrt{D_{tlw}/(\rho H)}$ and $\eta_{\max} \propto h_0$ (equation (15)), confirming a single-mode TLW regime. For larger amplitudes ($\hat{h}_0$), $\eta_{\max}$ continues to increase but tends to saturate, owing to the exhaustion of resonant amplification (primarily through vertical leakage of energy and momentum and transfer to harmonics, as discussed later); this saturation occurs much earlier and at substantially lower levels for $\hat{H} = 0.54$ ($\eta_{\max} \approx 170$ m at $\hat{h}_0 \approx 0.25$) than for $\hat{H} = 0.7$ ($\eta_{\max} \approx 400$ m at $\hat{h}_0 \approx 0.55$). Note that for $\hat{H} = 0.7$, over the interval $\hat{h}_0 = 0.1$–0.55, expression (15) must be modified in order for $\eta_{\max}$ to match the plateau associated with saturation of the amplitude growth (i.e. exhaustion of resonant gain). In that case, a curve of the form

$$\eta_{\max} = C\hat{h}_0 \left(1 - \alpha \hat{h}_0^2\right), \tag{22}$$

is suggested, where α is a constant to be fitted.

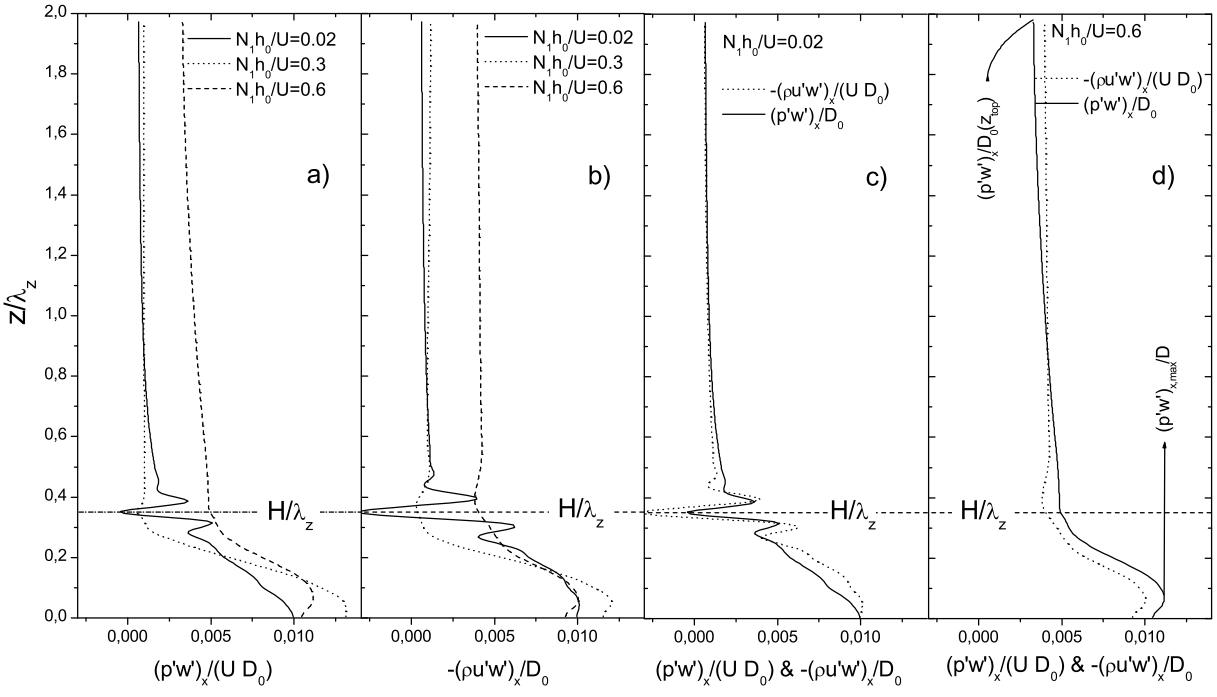

Figure 6. (a) Energy flux $\overline{p'w'}_x(z)$ for different values of $\hat{h}_0$ (case $\hat{H} = 0.7$). (b) As in panel (a) but for the momentum flux $-\rho, \overline{u'w'}_x(z)$. (c) Comparison of $\overline{p'w'}_x(z)$ and $-\rho, \overline{u'w'}_x(z)$ under linear conditions. (d) As in panel (c) but under nonlinear conditions. As an illustration, panel (d) shows both the maximum value of S_{pw} and its value at z_{top} (see expression (9)). The profiles $\overline{p'w'}_x(z)$ and $-\rho\overline{u'w'}_x(z)$ are normalised by UD_0 and D_0, respectively.

Corresponding profiles used to compare the vertical structure of energy and momentum transports and to assess the persistence of their coupling as nonlinearity increases. As an illustration, panel (d) shows both the maximum value of S_{pw} and its value at z_{top} (see expression (9)).

https://doi.org/10.5194/egusphere-2026-40
Preprint. Discussion started: 15 January 2026

The dependence of $\eta_{\max}/h_0$ on $\hat{h}_0$ (Figure 5d) shows that, relative to the linear extrapolation, TLWs lose amplitude over the entire range of $\hat{h}_0$ in both cases. As expected, this occurs much earlier and more abruptly for $\hat{H} = 0.54$, except for $\hat{H} = 0.7$ over $\hat{h}_0 = 0.02$–0.25 (very weak nonlinearity), where $\eta_{\max}/h_0$ exhibits a maximum at $\hat{h}_0 \approx 0.1$, about 10% above the linear reference value. This interval and the position of the maximum coincide exactly with those of the D_{tlw}/D_0 curve in Figure 2d, so the association between $\eta_{\max}/h_0$ and D_{tlw}/D_0 is evident. Moreover, comparing Figures 2d and 5d shows that the monotonic decrease of $\eta_{\max}/h_0$ and D_{tlw}/D_0 is very similar up to $\hat{h}_0 \approx 0.55$. Therefore, $\hat{h}_0 = 0.02$–0.25 is an interval in which resonant gain is particularly relevant for $\hat{H} = 0.7$.

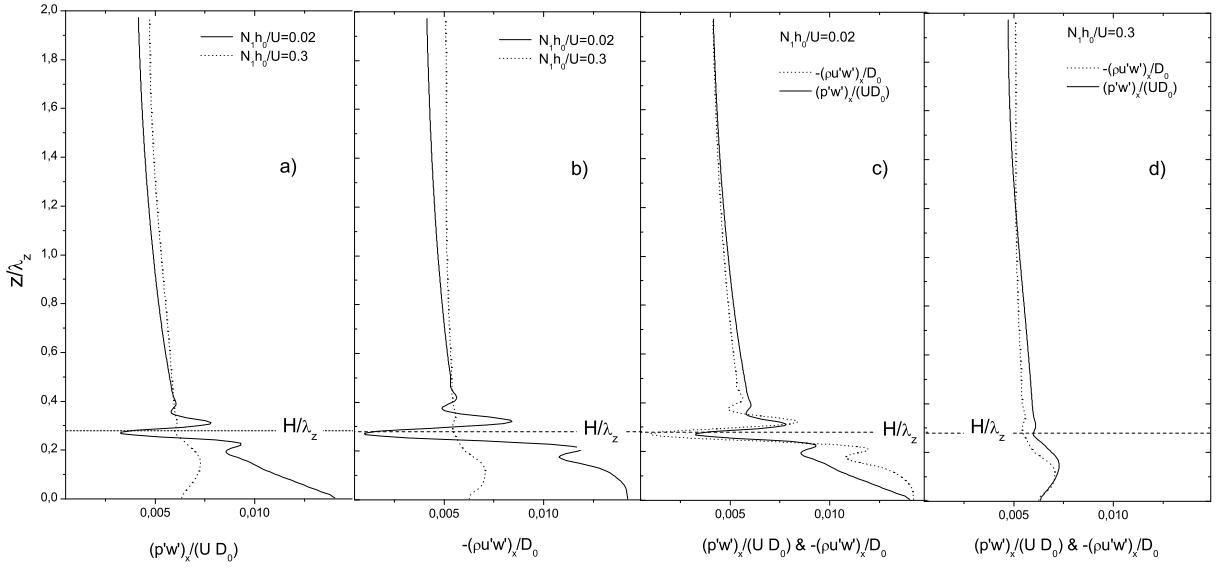

Figure 7. As in Figure 6, but for $\hat{H} = 0.54$.

The position diagnostics in Figures 5(e,f) complete the modal picture by distinguishing a displacement maximum, anchored within the TLW waveguide, from a maximum dominated by downstream PWs. For $\hat{H} = 0.7$, $z_{\eta_{\max}}/H$ remains close to unity up to $\hat{h}_0 \approx 0.5$, indicating that the maximum remains waveguide-anchored prior to the jump + secondary-train reorganisation, while $x_{\eta_{\max}}/a$ increases smoothly with step-like changes associated with that reorganisation. For $\hat{H} = 0.54$, $z_{\eta_{\max}}/H$ increases much earlier and $x_{\eta_{\max}}/a$ is large from the outset and varies little, suggesting a maximum associated primarily with downstream PWs rather than with a well-defined trapped waveguide; this helps explain why D_{pw} dominates already from $\hat{h}_0 \approx 0.1$ in Figure 2(c).

A key feature of Figures 6 and 7 is the strong oscillation of $\overline{p'w'}_x(z)$ and $-\rho\overline{u'w'}_x(z)$ near $z = H$ in the near-linear case ($\hat{h}_0 = 0.02$). This reflects standing vertical trapped modes within the waveguide formed by superposition of upward and downward propagating components reflected at $z = H$ and at the ground; under partial resonance, the profiles exhibit nodes, antinodes and sign reversals, as predicted by linear theory.

https://doi.org/10.5194/egusphere-2026-40
Preprint. Discussion started: 15 January 2026

For $\hat{H} = 0.7$ (Figure 6(a,b)), the near-linear profiles exhibit well-defined maxima within the waveguide and an approximately exponential decay above H, as expected from linear theory. As $\hat{h}_0$ increases (0.3–0.6), the maxima shift slightly upward and broaden, and the decay above H becomes more gradual, indicating a redistribution of flux into harmonic structures and/or partially propagating, upward-radiating components above the waveguide. Even so, most of the energy and momentum flux remains concentrated within the waveguide, consistent with D_{tlw} remaining dominant (Figure 2(d)).

For $\hat{H} = 0.54$ (Figure 7(a,b)), similar changes occur at smaller $\hat{h}_0$, consistent with a low-efficiency waveguide. By $\hat{h}_0 = 0.3$, the internal maxima lie closer to H and the profiles exhibit a markedly more gradual decay above H than in the near-linear regime and than in the $\hat{H} = 0.7$ case, indicating stronger leakage to levels above the waveguide and helping to explain the rapid degradation of D_{tlw} and the inability of the total drag to approach its linear reference (see Figure 2c).

Figures 6(c–d) and 7(c–d) show that, even at finite amplitude, the appropriately normalised energy and momentum flux profiles retain a surprisingly similar structure, which motivates the use of $C_u(z)$ and $\overline{C_u}$ (equations 12 and 13). In the linear limit, $\overline{p'w'}_x(z)/(UD_0)$ and $-\rho\overline{u'w'}_x(z)/D_0$ are nearly indistinguishable throughout the waveguide, implying $C_u(z) \approx U$ where the mode is well trapped.

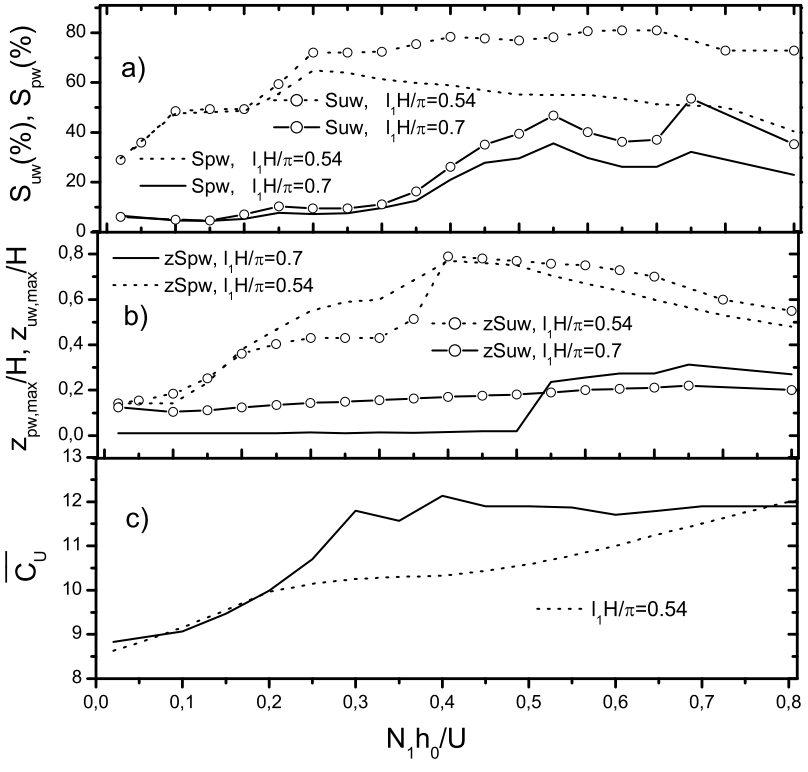

Figure 8. (a) Fractional leakage for energy and momentum, S_{pw} and S_{uw}, versus $\hat{h}_0$ for $\hat{H} = 0.54$ and $\hat{H} = 0.70$. (b) Location of maxima of S_{pw} and S_{uw} for $\hat{H} = 0.54$ and $\hat{H} = 0.70$. (c) Mean energy–momentum coupling measure $\overline{C}_u$.

At larger amplitude (e.g. $\hat{h}_0 = 0.6$ for $\hat{H} = 0.7$ and $\hat{h}_0 = 0.3$ for $\hat{H} = 0.54$), modest offsets and differences in decay rates appear, but the global similarity persists, so $\overline{C_u}$ remains close to U (mean deviations $< 10\%$), indicating that energy and momentum transports remain strongly coupled on average even as confinement degrades.

Figures 8(a–b) quantify the contrast using S_{pw}, S_{uw} and the vertical locations of their maxima: for $\hat{H} = 0.54$ leakage increases early and the maxima rise above the waveguide, whereas for $\hat{H} = 0.7$ leakage increases later and the maxima remain anchored near H until $\hat{h}_0 \approx 0.5$. Figure 8(c) shows that C_u remains close to U (mean deviations $< 10\%$), so the mean energy–momentum relationship largely retains its linear character even when confinement and TLW/PW partition change markedly.

https://doi.org/10.5194/egusphere-2026-40
Preprint. Discussion started: 15 January 2026

Together, S_{pw}, S_{uw} and $\overline{C_u}$ show that energy and momentum leak in comparable proportions across most of the range: S_{pw} and S_{uw} remain of similar magnitude without a significant offset.

These mechanisms explain the drag behaviour in Figure 2. For $\hat{H} = 0.7$, the waveguide remains highly efficient: despite increasing $\hat{h}_0$ (and the associated growth of dissipation and vertical radiation), a substantial fraction of the response remains trapped.

At weak amplitude, near-linear TLWs maximise D_{tlw}; at intermediate amplitude, detuning and saturation reduce the trapped contribution and produce the intermediate minimum in D/D_0; at larger amplitude, a jump-like reorganisation and the emergence of a coherent secondary trapped train (Figures 3 and 5) together with a moderate increase in the PW contribution (Figures 6 and 8) allow more efficient conversion of increased h_0 into momentum flux, so that D/D_0 exceeds the linear reference, with D_{tlw} still dominant but accompanied by a non-negligible D_{pw}.

For $\hat{H} = 0.54$, the waveguide is inefficient and does not sustain robust trapped resonance as $\hat{h}_0$ increases. TLWs are effective only in the near-linear limit (hence the early maximum in D_{tlw}), after which the train loses coherence: $\eta_{\max}/h_0$ saturates early, λ becomes ill-defined, and the flux profiles extend higher above H, consistent with stronger PW contributions. Consequently, D_{tlw}/D_0 decreases almost monotonically, D_{pw}/D_0 becomes dominant, and the total drag remains below the linear extrapolation.

In summary, the central message is that the evolution of the total drag and its components with increasing $\hat{h}_0$ is controlled not only by TLW amplitude, but above all by waveguide guiding efficiency, which determines whether energy extracted from the incident flow is largely retained and recycled within the trapped mode—allowing jump-driven reorganisation and a secondary trapped train, or whether it is transferred earlier to propagating components and/or to processes associated with detuning, saturation and eventual turbulent dissipation.

Finally, it is important to mention that the present study aims to isolate free-atmosphere internal-wave dynamics, in particular trapped lee waves (TLWs), rather than boundary-layer processes near the surface. We therefore adopt an idealised external-flow framework, treating the flow aloft as approximately inviscid and imposing a free-slip lower boundary to avoid introducing frictional stresses and boundary-layer parameterisation effects that are not central to the mechanisms of interest. This is consistent with the classical boundary-layer perspective in which a thin near-surface region is frictionally controlled, whereas the outer flow above can be approximated as inviscid to leading order. Under this idealisation, rotors and flow separation are not expected, since they depend critically on frictional vorticity generation within a realistic boundary layer; the drag response is thus interpreted mainly in terms of wave-internal processes (detuning, harmonic generation, reorganisation and leakage). A no-slip (or stress-imposing) lower boundary would only be required if the focus were on rotor/separation dynamics or strongly dissipative breaking governed by surface stress, which lies beyond the scope of the present set-up.

7 Conclusion

This study investigated how pressure drag in non-hydrostatic, stably stratified flow over a bell-shaped ridge evolves with nonlinearity in a two-layer atmosphere. Nonlinearity was varied exclusively through the mountain height h_0 (equivalently

https://doi.org/10.5194/egusphere-2026-40
Preprint. Discussion started: 15 January 2026

$\hat{h}_0 = l_1 h_0$), while N_1, N_2, H, and U were held fixed. The simplicity of the atmospheric configuration used in this theoretical model allows a clearer isolation of the complex effects linked to nonlinearity.

Two configurations were considered, guided by the linear framework of Teixeira et al. 2013a: (i) a case in which trapped-lee-wave drag dominates in the linear reference, and (ii) a case in which trapped-lee-wave and propagating-wave contributions are of comparable magnitude. Diagnostics based on wave amplitude, wavelength, leakage of energy and momentum fluxes, and retuning were used to interpret the nonlinear response.

For the high-efficiency waveguide configuration ($\hat{H} = 0.70$), a substantial fraction of the response remains trapped over a broad range of $\hat{h}_0$. At small amplitudes, modest nonlinear effects can enhance resonance and increase D_{tlw}. With increasing $\hat{h}_0$, detuning, harmonic generation, and leakage reduce trapped-wave coherence and produce an intermediate minimum in D/D_0. At larger amplitudes, the flow reorganises and a secondary trapped-wave train can re-emerge downstream, while a growing propagating-wave contribution coexists with still-dominant TLW drag.

For the low-efficiency waveguide configuration ($\hat{H} = 0.54$), trapped waves are robust only in the near-linear regime. As $\hat{h}_0$ increases, trapped-wave coherence degrades rapidly, leakage to propagating components increases, and D_{tlw} collapses while D_{pw} becomes dominant. Consequently, the total drag remains below the linear extrapolation across the explored range.

Despite these pronounced differences in TLW/PW partition, the mean energy - momentum coupling within the waveguide remains close to its linear character, with $\overline{C}_u$ typically remaining near U. The results therefore indicate that the evolution of total drag with nonlinearity is controlled not only by TLW amplitude, but also and primarily by the waveguide guiding efficiency, which determines whether the energy extracted from the incident flow is retained and recycled within trapped modes or transferred early to propagating components and saturation processes.

These findings may be relevant for improving orographic-drag parametrisation in weather and climate models by highlighting regimes in which trapped-wave drag can be significant and by clarifying how nonlinear effects alter the partition between trapped and propagating contributions.

https://doi.org/10.5194/egusphere-2026-40
Preprint. Discussion started: 15 January 2026

References

Argain, J. L., Miranda, P. M. A., and Teixeira, M. A. C.: Estimation of the friction velocity in stably stratified boundary layer flows over hills, Boundary-Layer Meteorol., 130, 15–28, 2009.

Doyle, J. D. and Coauthors: An intercomparison of T-REX mountain-wave simulations and implications for mesoscale predictability, Mon. Weather Rev., 139, 2811–2831, 2011.

Durran, D. R.: Mountain Waves and Downslope Winds, in: Atmospheric Processes over Complex Terrain, Meteorological Monographs, Vol. 23, American Meteorological Society, Boston, MA, 59–81, 1990.

Leutbecher, M.: Surface pressure drag for hydrostatic two-layer flow over axisymmetric mountains, J. Atmos. Sci., 58, 797–807, 2001.

Lilly, D. K. and Klemp, J. B.: The effects of terrain shape on nonlinear hydrostatic mountain waves, J. Fluid Mech., 95, 241–261, 1979.

Lott, F.: A study of the low frequency inertio-gravity waves observed during PYREX, J. Geophys. Res., 103, 1747–1757, 1998.

Lott, F. and Teixeira, M. A. C.: A new theory for downslope windstorms and trapped mountain waves, J. Atmos. Sci., 73, 3585–3597, 2016.

McFarlane, N. A.: The effect of orographically excited gravity-wave drag on the general circulation of the lower stratosphere and troposphere, J. Atmos. Sci., 44, 1775–1800, 1987.

Miranda, P. M. A. and James, I. N.: Non-linear three-dimensional effects on gravity-wave drag: splitting flow and breaking waves, Q. J. Roy. Meteor. Soc., 118, 1057–1081, 1992.

Olafsson, H. and Bougeault, P.: Nonlinear flow past an elliptic mountain ridge, J. Atmos. Sci., 53, 2465–2489, 1996.

Peltier, W. R. and Clark, T. L.: Nonlinear mountain waves in two and three spatial dimensions, Q. J. Roy. Meteor. Soc., 109, 527–548, 1983.

Phillips, D. S.: Analytical surface pressure and drag for linear hydrostatic flow over three-dimensional elliptical mountains, J. Atmos. Sci., 41, 1073–1084, 1984.

Sawyer, J. S.: Numerical calculation of the displacements of a stratified airstream crossing a ridge of small height, Q. J. Roy. Meteor. Soc., 86, 326–345, 1960.

Scorer, R. S.: Theory of waves in the lee of mountains, Q. J. Roy. Meteor. Soc., 75, 41–56, 1949.

Shutts, G. J. and Gadian, A.: Numerical simulations of orographic gravity waves in flows which back with height, Q. J. Roy. Meteor. Soc., 125, 2743–2765, 1999.

Smith, R. B.: The influence of mountains on the atmosphere, Adv. Geophys., 21, 87–230, 1979.

Smith, R. B.: Hydrostatic airflow over mountains, Adv. Geophys., 31, 1–41, 1989.

Stensrud, D. J.: Parametrization Schemes: Keys to Understanding Numerical Weather Prediction Models, Cambridge University Press, Cambridge, UK, 2009.

Teixeira, M. A. C. and Miranda, P. M. A.: Linear criteria for gravity-wave breaking in resonant stratified flow over a ridge, Q. J. Roy. Meteor. Soc., 131, 1815–1820, 2005.

Teixeira, M. A. C. and Miranda, P. M. A.: A linear model of gravity wave drag for hydrostatic sheared flow over elliptical mountains, Q. J. Roy. Meteor. Soc., 132, 2439–2458, 2006.

Teixeira, M. A. C., Miranda, P. M. A., and Argain, J. L.: Mountain waves in two-layer sheared flows: critical level effects, wave reflection, and drag enhancement, J. Atmos. Sci., 65, 1912–1926, 2008.

Teixeira, M. A. C., Argain, J. L., and Miranda, P. M. A.: Drag produced by trapped lee waves and propagating mountain waves in a two-layer atmosphere, Q. J. Roy. Meteor. Soc., 139, 964–981, 2013.

https://doi.org/10.5194/egusphere-2026-40
Preprint. Discussion started: 15 January 2026

Teixeira, M. A. C., Argain, J. L., and Miranda, P. M. A.: Orographic drag associated with lee waves trapped at an inversion, J. Atmos. Sci., 70, 2930–2947, 2013.

Vosper, S. B.: Inversion effects on mountain lee waves, Q. J. Roy. Meteor. Soc., 130, 1723–1748, 2004.

Acknowledgements. The author used an AI-based language assistant to improve the clarity and grammar of the English text. All scientific content, analyses, and conclusions were conceived and verified by the author.

Competing interests. The author declares that no competing interests are present.